Numerical modeling of artificial ionospheric layers driven by high-power HF heating

B. Eliasson,[1,2] X. Shao,[1] G. Milikh,[1] E. V. Mishin,[3] and K. Papadopoulos[1]

Received 12 July 2012; revised 9 August 2012; accepted 14 August 2012; published 19 October 2012.

[1] We present a multi-scale dynamic model for the creation and propagation of artificial plasma layers in the ionosphere observed during high-power high-frequency (HF) heating experiments at HAARP. Ordinary (O) mode electromagnetic (EM) waves excite parametric instabilities and strong Langmuir turbulence (SLT) near the reflection point. The coupling between high-frequency electromagnetic and Langmuir waves and low-frequency ion acoustic waves is numerically simulated using a generalized Zakharov equation. The acceleration of plasma electrons is described by a Fokker-Planck model with an effective diffusion coefficient constructed using the simulated Langmuir wave spectrum. The propagation of the accelerated electrons through the non-uniform ionosphere is simulated by a kinetic model accounting for elastic and inelastic collisions with neutrals. The resulting ionization of neutral gas increases the plasma density below the acceleration region, so that the pump wave is reflected at a lower altitude. This leads to a new turbulent layer at the lower altitude, resulting in a descending artificial ionized layer (DAIL), that moves from near 230 km to about 150 km. At the terminal altitude, ionization, recombination, and ambipolar diffusion reach equilibrium, so the descent stops. The modeling results reproduce artificial ionospheric layers produced for similar sets of parameters during the high-power HF experiments at HAARP.

Citation: Eliasson, B., X. Shao, G. Milikh, E. V. Mishin, and K. Papadopoulos (2012), Numerical modeling of artificial ionospheric layers driven by high-power HF heating, *J. Geophys. Res.*, *117*, A10321, doi:10.1029/2012JA018105.

1. Introduction

[2] Ordinary (O) mode electromagnetic (EM) waves can deposit significant amount of energy to the plasma when their frequency matches either the local plasma frequency, the upper hybrid frequency, or the frequency of Bernstein modes near multiples of the electron cyclotron frequency [e.g., *Gurevich*, 1978]. This energy can heat the bulk electrons to a few thousand degrees above the ambient temperature and produce suprathermal electrons in the range a few tens of electron volts. Suprathermal electrons can ionize neutral gas if the electron energy exceeds the ionizing potential 12–18 eV [e.g., *Schunk and Nagy*, 2000]. A concept of using high-power EM waves to ionize the neutral gas and create artificial ionospheric layers has been widely discussed in the past [e.g., *Koert*, 1991]. In particular, *Carlson* [1993] noted that artificial ionization would occur at the effective radiated power (ERP) $P_0 \sim 1$ GW, similar to that of the solar ultraviolet radiation creating the natural F-region ionosphere. Indeed, significant ionospheric ionization due to high-frequency (HF) heating was achieved when the upgraded High-Frequency Active Auroral Research Program (HAARP) facility provided ERP up to 4 GW. On the other hand, thermal heating of the electrons by the EM wave can also lead to large-scale density modifications and cavity formation in the ionosphere, resulting in a focusing of the EM beam and further intensification of the heating [*Hansen et al.*, 1990].

[3] The initial high-power HF heating experiments at HAARP [*Pedersen et al.*, 2009] showed indications of enhanced plasma densities near 200 km altitude, which apparently de-focused the transmitter beam into a ring surrounding a bright central spot visible in optical measurements [cf. *Kosch et al.*, 2004]. Later, *Pedersen et al.* [2010] observed artificial ionospheric plasma layers descending during the heating. The HF-driven ionization processes in the ionospheric F region were initiated near 220 km altitude. When the artificial plasma reached sufficient density to reflect the transmitter beam, it rapidly descended to about 150 km altitude. *Mishin and Pedersen* [2011] explained the descending artificial ionized layer (DAIL) in terms of an ionizing wavefront created due to suprathermal electron acceleration by HF-excited strong Langmuir turbulence (SLT) in the O mode critical layer. As long as the high-energy electrons ionize the neutral gas below the reflection point faster than the electrons are lost due to

[1]Department of Physics and Department of Astronomy, University of Maryland, College Park, Maryland, USA.
[2]Institute for Theoretical Physics, Faculty of Physics and Astronomy, Ruhr University Bochum, Bochum, Germany.
[3]Space Vehicles Directorate, Air Force Research Laboratory, Kirtland Air Force Base, Albuquerque, New Mexico, USA.

Corresponding author: B. Eliasson, Institute for Theoretical Physics, Faculty of Physics and Astronomy, Ruhr University Bochum, Universitätsstr. 150, DE-44780 Bochum, Germany. (bengt@tp4.rub.de)

0148-0227/12/2012JA018105

recombination and diffusion, the artificial ionospheric layer moves downward.

[4] The results emphasized the need for a comprehensive numerical model of HF-induced electron acceleration and its impact on the ionosphere. The model should include the generation of plasma turbulence, collisionless electron acceleration, transport of the accelerated electrons, and collisional interactions with neutrals. It is the objective of this paper to create such a model and quantitatively describe the development of artificial ionization in the F-region ionosphere due to high-power O mode waves.

[5] The paper is organized as follows. In section 2, we develop a model for resonant electron acceleration and heating by HF-induced SLT. This model includes (1) a full-scale numerical model and (2) a Fokker-Planck code. The first code simulates the SLT generation and derives the effective diffusion coefficient from the Langmuir spectrum. This serves as the input for the second code, which simulates the formation of the high-energy tail in the electron distribution due to wave-particle interactions. Section 3 describes the transport and collisional degradation of the fast (tail) electrons by means of a kinetic flux model. Section 4 presents a chemical evolution model for the electrons and the ion species, where the ionization is driven by the fast electrons and balanced by recombination and diffusion. As the new plasma builds up, the matching condition for the O mode is reached at a lower altitude, resulting in the creation and descent of the artificial ionospheric layer. Numerical simulations of the dynamic model show good comparison with the observations. The results are summarized and discussed in section 5.

2. Modeling HF-Excited SLT and Electron Acceleration

[6] We develop a numerical model for the resonant interaction and acceleration of electrons by SLT near the turning point z_O of the O mode pump wave, where the pump frequency f_0 matches the local electron plasma frequency f_p. The turbulence is simulated by means of a full wave model [*Eliasson*, 2008a, 2008b; *Eliasson and Stenflo*, 2008, 2010]. The simulation code uses a one-dimensional geometry, along the z-axis, starting at an altitude of 142 km and ending at 342 km. Our simulation code is based on a nonuniform nested grid method [*Eliasson*, 2008a; *Eliasson and Stenflo*, 2010]. While the electromagnetic radiation field is represented on a fixed grid with grid size 4 m everywhere, the electrostatic field and particle dynamics are resolved with a much denser grid of grid size $\delta z = 4$ cm locally, at $z = 229.5$–231.5 km (and also at the topside, at $z = 252.5$–254.5 km), in order to resolve small-scale structures and electrostatic turbulence at the critical layer. Outside this region, all quantities are resolved on the 2-meter grid. This nested grid procedure is used to avoid a severe Courant-Friedrich-Levy (CFL) condition on the time-step, $\delta t \lesssim \delta z/c$, which would appear if the electromagnetic field would be resolved on the dense grid [*Eliasson*, 2008a]. Small, random density fluctuations are added to seed the parametric instability in the plasma. We use oxygen ions so that $m_i = 16\, m_p$ where m_p is the proton mass. A 4th-order Runge-Kutta algorithm is used to advance the solution in time, with time step $\delta t = 1.6 \times 10^{-8}$ s. In this model, O mode polarized (left-hand polarized relative to the downward-directed magnetic field $\mathbf{B}_0$) EM pump waves are injected vertically from the bottomside at 142 km, by setting the $\mathbf{E} = (\hat{\mathbf{x}} + i\hat{\mathbf{y}})E_O$ on the upward propagating field ($\hat{\mathbf{x}}$ and $\hat{\mathbf{y}}$ are the unit vectors along the x- and y-axes). The magnetic field with magnitude $B_0 = 5 \times 10^{-5}$ is tilted $\chi = 14^\circ$ to the vertical z-axis in the x-z plane, in accordance with the HAARP conditions. The ionospheric density profile is assumed to be of the form $n_{i0}(z) = n_{0,\max} \exp\left[-(z - z_{\max})^2/L_{n0}^2\right]$, where $n_{0,\max} = 1.436 \times 10^{11}$ m^{-3} is the electron density at the F_2 peak located at $z_{\max} = 242$ km, and $L_{n0} = 31.62$ km is the ionospheric scale length. The F_2-peak electron density corresponds to the peak plasma frequency $f_{oF_2} = 3.41$ MHz, while the pump frequency is taken $f_0 = 3.2$ MHz ($\omega = 20.1 \times 10^6$ s^{-1}). For the chosen parameters, the turning point $n_o = n_c = 1.26 \times 10^5$ cm^{-3} is at $z_O \approx 230.6$ km, where the local plasma length scale is $L_n = 1/(d\ln n_0/dz)|_{z_0} = 43$ km.

[7] The generalized Zakharov model couples the EM and Langmuir waves to the low-frequency ion acoustic wave, giving rise to parametric instabilities and SLT [e.g., *Eliasson and Stenflo*, 2010]. The model also includes ion and electron Landau damping. It turns out that direct mode conversion of the EM wave to electrostatic waves via resonant absorption is inefficient for normal incidence, and is important only for oblique propagation close to the Spitze angle $\chi_c = \arcsin\left[Y^{1/2}(1+Y)^{-1/2}\sin\chi\right]$ where $Y = \omega_{ce}/\omega_{pe}$. For normal incidence, the fraction T of the incident energy that is linearly converted is given by equation (18) of *Mjølhus* [1990] with $N_x = N_y = 0$. For small values of χ and for $\omega_{ce} < \omega_{pe}$, it can be roughly estimated as $T = \exp\left(-\pi^2\, Y^{-1/2} d/\lambda_0\right)$, where $d = L_n Y^2 \sin^2\chi$ is the distance between the cutoffs of the O mode and upper hybrid wave, and λ_0 is the vacuum wavelength of the EM wave. For our parameters, with $L_n = 43$ km, Y = 0.4, $\chi = 14^\circ$ and $\lambda_0 = 100$ m, we obtain $d = 400$ m and $T = 10^{-29}$, which is negligible. On the other hand, after the instability has been taking place and SLT has created small-scale density fluctuations, the mode conversion is much more efficient. Figure 1 shows the simulation results for a pump wave amplitude $E_O = 1.5$ V/m and the ion (electron) temperature $T_i = 0.2$ eV ($T_e = 0.4$ eV). Clearly, intense electrostatic waves (the z component E_z) and ion density fluctuations n_i are generated near the turning point $z_O = 230.6$ km. Note the different scales for $E_{x,y}$ and E_z. The traces above 230 km are due to the partial conversion into the Z mode, which for the given conditions can propagate to the topside and generate electrostatic turbulence near the transformation point [e.g., *Mjølhus*, 1990].

[8] The large-amplitude z-component of the electric field near z_O appears due to the development of SLT near z_O, which is manifested by solitary wave packets trapped in ion density cavities [e.g., *DuBois et al.*, 1990; *Mjølhus et al.*, 2003]. Figure 2 shows the spatial structure of the electric field and density in the vicinity of z_O. The solitary waves and cavities of widths $d_s \approx (15 - 25) r_D \approx 0.3$–0.5 m are spaced apart by $\delta l_s \approx 1$–2 m ($r_D \approx 2$ cm is the Debye radius). While the O mode continues to pump energy, the system reaches a dynamic equilibrium between the long-scale pumping and short-scale absorption due to nonlinear transfer of the wave

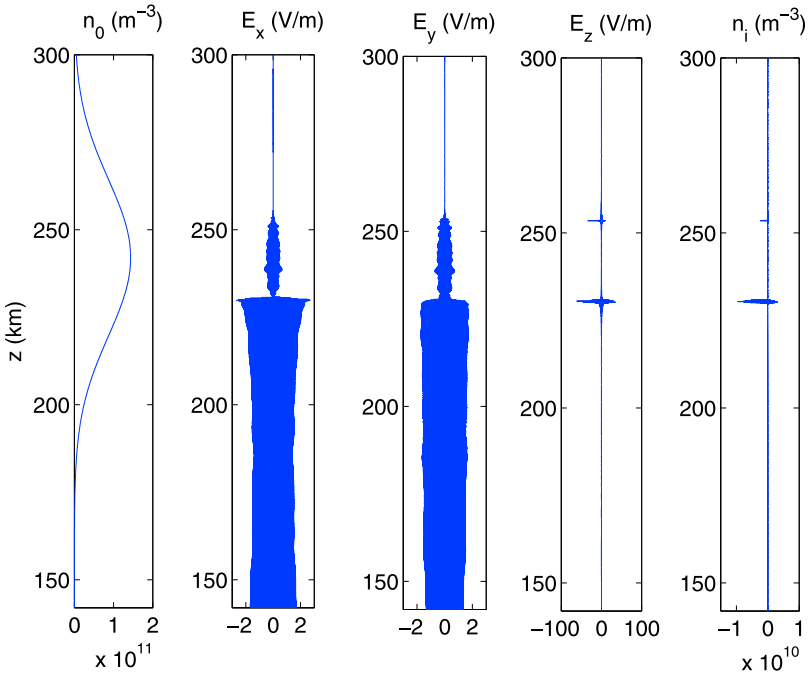

Figure 1. From left to right: The altitude profile of the ambient F-region density, electric field components, and ion density fluctuations for $E_O = 1.5$ V/m.

energy by collapsing wave packets [e.g., *Galeev et al.*, 1977]. Similar results are obtained for pump amplitudes $E_O = 1$ and 2 V/m. Figure 3 illustrates that both the size of the turbulent region z and the amplitude of the electrostatic waves increase with increasing amplitude of the pump wave.

[9] The short-scale (low-phase speed) Langmuir waves interact resonantly with electrons, which are stochastically accelerated, leading to electron diffusion in velocity space and formation of a high-energy tail in the electron distribution function. This process and transport of the electrons through the turbulent region can be modeled by a Fokker-Planck equation for the averaged 1D (along $\mathbf{B}_0$) electron distribution [e.g., *Sagdeev and Galeev*, 1969]

$$\frac{\partial F}{\partial t} + v\frac{\partial F}{\partial z} = \frac{\partial}{\partial v} D(v) \frac{\partial F}{\partial v} \tag{1}$$

with diffusion coefficient $D(v)$

$$D(v) = \frac{\pi e^2}{m_e^2} \frac{W_k\left(\omega, \frac{\omega}{v}\right)}{|v|} \tag{2}$$

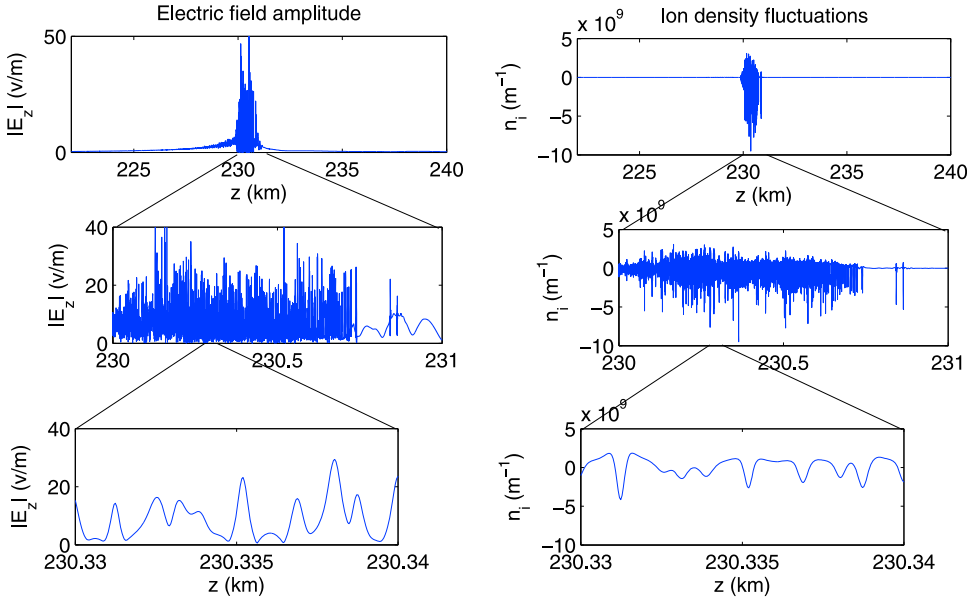

Figure 2. The amplitude of E_z and slowly varying ion density fluctuations n_i at various altitudes, for $E_O = 1.5$V/m.

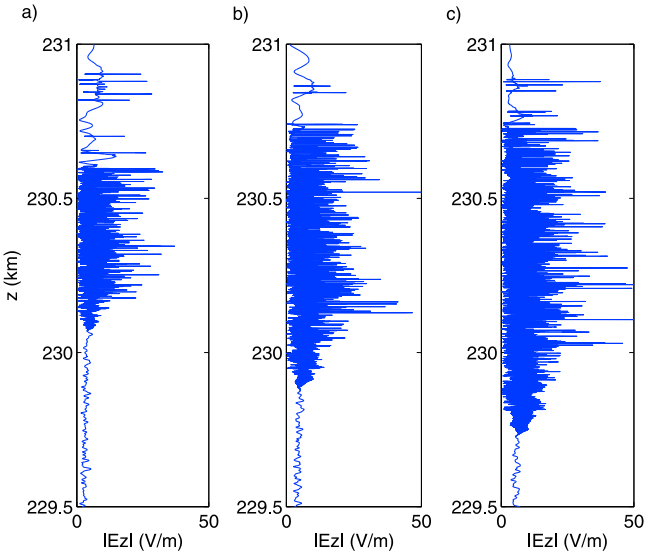

Figure 3. The z component of the electrostatic field near z_O for E_O = (a) 1 V/m, (b) 1.5 V/m and (c) 2 V/m.

where $W_k(\omega, \mathrm{k}) = \Delta E^2/\Delta k$ is the spectral energy density of the electric field per wavenumber Δk, and ΔE^2 is the differential squared electric field. Here, W_k is in V^2/m and normalized such that

$$\int W_k\, dk = \frac{1}{\Delta z}\int_{z_0}^{z_0+\Delta z} E_z^2\, dz. \tag{3}$$

Note that the integration in the r.h.s. of equation (3) is over the turbulent region $z_0 - z_0 + \Delta z$, i.e. 230.105–230.625, 229.945–230.745, and 229.745–230.745 km for E_O = 1, 1.5, and 2 V/m, respectively (see Figure 3). Figure 4 shows the spectral density $\mathrm{W_k}(\omega,\mathrm{k})$ and diffusion coefficient $D(v)$ calculated by taking the spatial Fourier transform of E_z in Figure 3 with ω fixed at the pump frequency.

[10] For numerical convenience, we have obtained the smoothed spectra and diffusion coefficients in Figure 5 by performing a convolution of W_k by a Gaussian $\left[1/(\kappa\sqrt{2\pi})\right]\exp[-k^2/(2\kappa^2)]$ with κ = 0.2 m^{-1}. At resonance $v = \omega/k$, large values of k correspond to small v and *vice versa.* In agreement with the SLT predictions [e.g., *Galeev et al.*, 1977; *Morales and Lee*, 1974; *Papadopoulos and Coffey*, 1974; *Manheimer and Papadopoulos*, 1975], the diffusion coefficients in Figures 4 and 5 indicate that only electrons with initial energies exceeding some minimum energy $\varepsilon_{\min}$ can be accelerated by SLT. The physics of the electron acceleration by localized Langmuir solitons is well understood. While electrons pass through a solitary wave packet, they gain or lose energy, depending on the phase of the oscillations. If the electron speed is smaller than the product $d_s\omega$, where d_s is the solitons width, electrons experience many oscillations while passing through the solitons. The net acceleration is small, since on average the positive and negative contributions cancel each other. In the opposite case, electrons experience one or a few oscillations across the soliton. This can lead to a significant net acceleration of the electron. Randomly distributed solitons in space will therefore give rise to effective electron diffusion in velocity space, similar to a random walk process.

[11] As a sanity check, we have derived an analytical model of the diffusion coefficient due to SLT comprising of non-propagating Langmuir solitons [e.g., *Zakharov*, 1984]

$$E_z^{(s)} = \frac{\phi_s}{d_s}\,\mathrm{sech}\left(\frac{z}{d_s}\right). \tag{4}$$

where $\phi_s = (2k_BT_e/e)\sqrt{6(3T_i/T_e+1)}$. For T_i = 0.2 eV and T_e = 0.4 eV, the value of ϕ_s is 2.65 V. This provides the

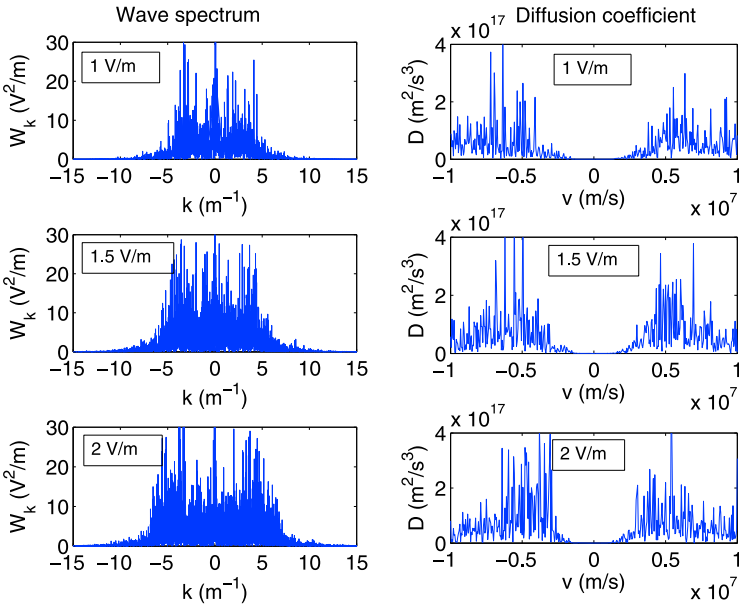

Figure 4. The wave spectrum and diffusion coefficients for (top) E_O = 1 V/m, (middle) E_O = 1.5 V/m and (bottom) E_O = 2 V/m.

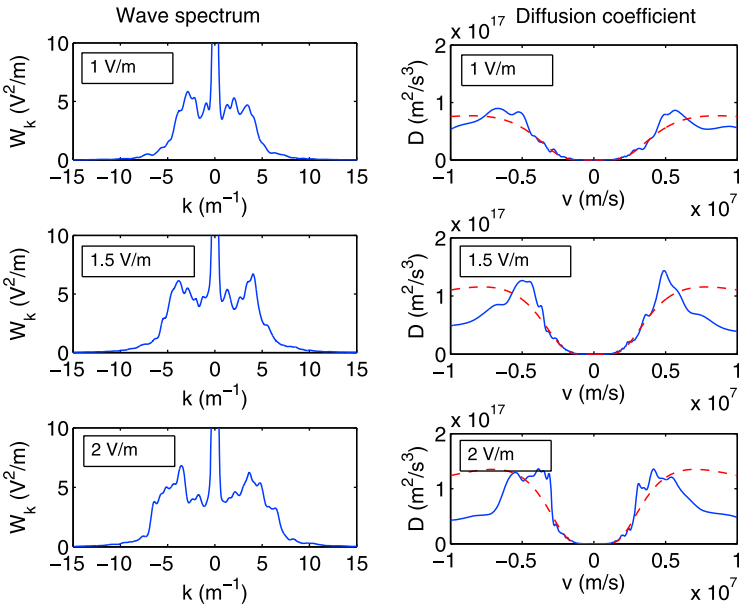

Figure 5. The convolved wave spectra and diffusion coefficients for E_O = (top) 1 V/m, (middle) 1.5 V/m, and (bottom) 2 V/m. The red dashed lines indicate the results of the analytical model (7) with the fitted coefficients N_s = 1.43 m^{-1} and d_s = 1.19 m.

peak amplitude of ≈15–20 V/m for $d_s \approx$ 0.13–0.20 m, consistent with the solitary wave packets in Figure 2. The Fourier transform of $E_z^{(s)}$ in space

$$E_k = \sqrt{\frac{\pi}{2}}\phi_s \,\mathrm{sech}\left(\frac{\pi d_s k}{2}\right) \tag{5}$$

is normalized so that $\int E_z^{(s)2} dx = \int E_k^2 dk$. Using an ensemble of solitons, we can estimate the average spectral density

$$W_k = N_s E_k^2 = \frac{N_s \pi \phi_s^2}{2}\,\mathrm{sech}^2\left(\frac{\pi d_s k}{2}\right), \tag{6}$$

where N_s is the average number of solitons per meter. The diffusion coefficient is

$$D(v) = \frac{\pi e^2}{m_e^2}\frac{W_k(\omega, \omega/k)}{|v|} = \frac{N_s \pi^2 e^2}{2m_e^2|v|}\phi_s^2\,\mathrm{sech}^2\left(\frac{\pi d_s \omega}{2v}\right). \tag{7}$$

In agreement with the above discussion, $D(v)$ vanishes at $|v| \ll d_s\omega$, when the net acceleration is supposed to be small. The input parameters of the analytical model are N_s, d_s, and ϕ_s. As an example, we have plotted the diffusion coefficient (7) in Figure 5 (indicated with red, dashed lines) for ϕ_s = 2.65 V, N_s = 1.43 m^{-1} and d_s = 1.19 m. It is seen that the analytical model is fairly close to the simulations at $|v| \le 6 \times 10^6$ m/s or energy $\varepsilon = m_e v^2/2 \le 100$ eV and significantly deviates only at $\varepsilon > 100$ eV for E_O = 1.5 and 2 V/m. Therefore, we conclude that the analytic model satisfactorily describes acceleration of the most significant part of the suprathermal electron population.

[12] Next, the convolved diffusion coefficients (such as in Figure 5) are used to solve equation (1) at various temperatures of the ambient electrons. The computational domain in velocity space is from -10^7 m/s to $+10^7$ m/s, resolved by 400 intervals, and in z-domain set by the width of the turbulent region (typically about 500 m to 1 km; see Figure 5), and resolved by 10 intervals. The solution is advanced in time with the standard 4th-order Runge-Kutta scheme with the time step 5×10^{-9} s. The ambient population is assumed Maxwellian with the distribution $F_M = 1/\left(\sqrt{2\pi}v_{Te}\right)\exp\left[-v^2/\left(2v_{Te}^2\right)\right]$ ($v_{Te} = \sqrt{k_B T_e/m_e}$ is the electron thermal speed). At the top (bottom) boundary, we use an inflow condition for negative (positive) velocities and an outflow condition for positive (negative) velocities. As an inflow condition, we set $F = F_M$ on the boundary, and as an outflow condition at the opposite boundary, we solve the Fokker-Planck equation (1) on the boundary. The electrons gain energy as they travel through the turbulent region. After some time, the equilibrium between inflow, outflow, and electron acceleration is established. Figure 6 shows the resulting electron distribution as a function of velocity and altitude. Electrons with negative velocities ($v < 0$) flow downwards and are gradually heated, resulting in a widening of the electron distribution function for negative velocities at the bottom boundary, and *vice versa* for electrons with positive velocities ($v > 0$) streaming upwards. This leads to an asymmetric electron distribution with high-energy tails streaming out from the heated region. It is clear from Figure 6 that only electrons with a large enough initial temperatures of about 0.4 eV and above are efficiently heated by the turbulence, while the electrons with temperature 0.2 eV are only slightly heated by the turbulence.

[13] To assess the validity of the Fokker-Planck scheme, we have compared it with direct test particle simulations,

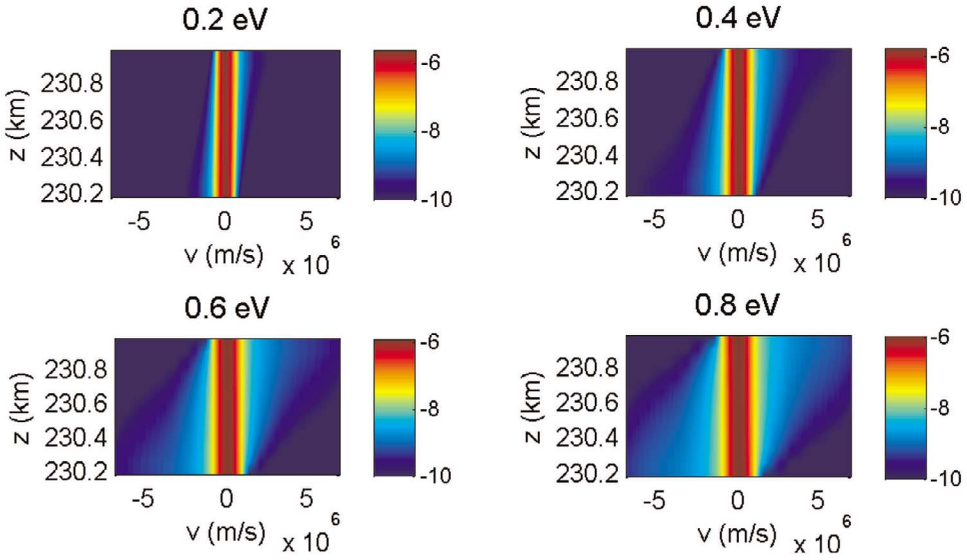

Figure 6. The electron velocity distribution function $F(v)$ (10-logarithmic scale) for $E_0 = 1.5$ V/m.

using the full electric field **E** from the generalized Zakharov simulations. The resulting energy distribution of the test particles, shown in Figure 7, agrees remarkably well with the energy distribution at the outflow boundary from the Fokker-Planck simulation. This justifies the use of the Fokker-Planck model, which is computationally much less demanding than the test-particle simulations.

[14] From the electron velocity distribution function, we obtain the energy distribution of electrons streaming out through the boundaries. Figure 8 shows (top) the electron energy distribution $F(\varepsilon) = F(v)dv/d\varepsilon$ and (bottom) the fraction of the population above the given energy $n_e^{hot}(\varepsilon) = \int_{\varepsilon}^{\infty} F(\varepsilon)d\varepsilon$ at the bottomside of the acceleration region for various electron temperatures (Figures 8a and 8b) and pump amplitudes E_0 (Figures 8c and 8d).

[15] It follows from Figure 8, the accelerated electron population is a very sensitive function of T_e and the pump amplitude E_0. In particular, minor changes of E_0 lead to significant modifications of the high-energy tail. The log-log plots in Figure 8 suggest that the main part of the accelerated distribution can be described parametrically by a power law $F(\varepsilon) \approx a\varepsilon^{-b}$ and $n_e^{hot} = a\varepsilon^{-b+1}/(b-1)$. This agrees well with the prior works [e.g., *Galeev et al.*, 1977, 1983; *Pelletier*, 1982; *Wang et al.*, 1997; *Gurevich et al.*, 2004]. However, in our case the SLT region is spatially bounded, and the acceleration time is limited by the electron residence time in the SLT region. As a result, the power-law parameters a and b depend on E_O, L_n, and T_e. Table 1 shows numerically fitted values of a and b in the range $2 \le \varepsilon \le 50$ eV for various inputs, using L_n = 40 km. Clearly, the value of b decreases for increasing pump amplitudes E_O and electron temperature T_e, leading to significant enhancement of the high-energy electron tail. The value of a increases with increasing T_e, but decreases with increasing E_O except from E_O = 1 to 1.5 V/m at T_e = 0.4 eV.

3. Flux Model for Hot Electrons

[16] The suprathermal, hot electrons streaming along the magnetic field lines degrade due to elastic and inelastic collisions with neutral atoms and molecules. *Gurevich et al.*

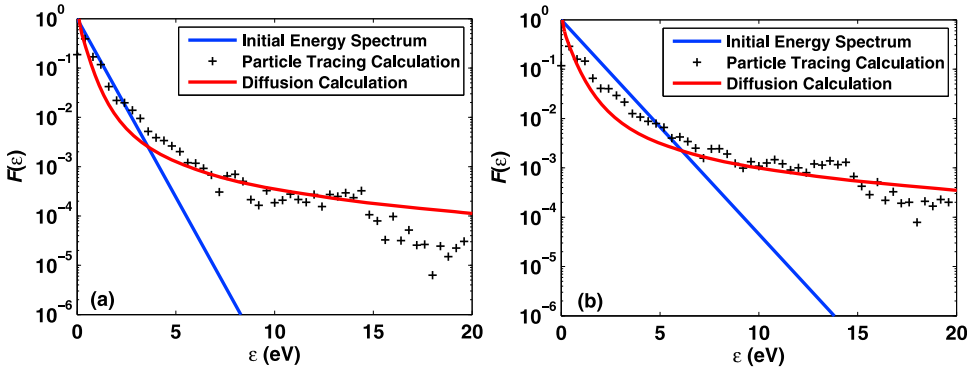

Figure 7. Comparison of electron distribution vs. energy between diffusion calculation and particle tracing with full electric field. Electron temperature: (a) 0.6 eV and (b) 1.0 eV.

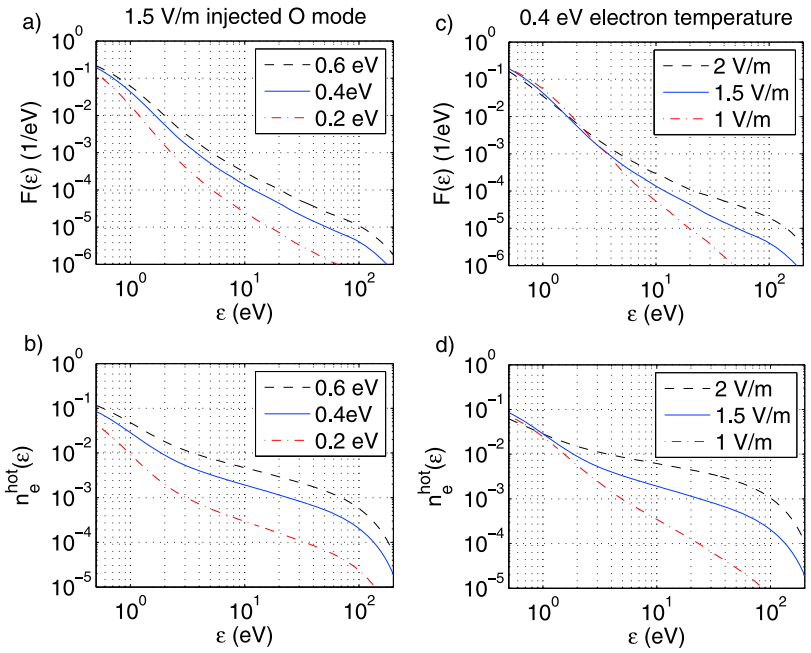

Figure 8. (top) The electron energy distribution $F(\varepsilon)$ and (bottom) the fraction of the population above the given energy $n_e^{hot}(\varepsilon)$ for various (a and b) T_e and (c and d) E_0.

[1985] showed that their distribution outside a thin accelerating layer can be approximated as

$$F^{hot}(\varepsilon, z) = F(\varepsilon) \exp\left(-\int_{z_o}^{z} \frac{dz}{L(z,\varepsilon)}\right), \tag{8}$$

where the collisional loss length $L(z,\varepsilon)$ is given by

$$L(z,\varepsilon) = \frac{1/\sqrt{3}}{\sqrt{N_O^2 \sigma_{tr}^O \sigma_{in}^O + N_{N_2}^2 \sigma_{tr}^{N_2} \sigma_{in}^{N_2} + N_{O_2}^2 \sigma_{tr}^{O_2} \sigma_{in}^{O_2}}} \tag{9}$$

and $F(\varepsilon)$ is obtained from the acceleration model (in the previous section) as a boundary condition at $z = z_0$. Here σ_{tr}^j is the transport cross-section for elastic collisions and σ_{in}^j is the cross-section for inelastic collisions with neutral species j.

[17] Figure 9 shows the energy spectra of the fast electrons at various altitudes above (Figure 9a) and below (Figure 9b) the acceleration region near $z_0 = 230$ km for $E_O = 1.5$ V/m and the ambient electron temperature $T_{e0} = 0.6$ eV. Note the different scales for $F(\varepsilon)$ in Figures 9a and 9b. As anticipated, the fast electrons rapidly degrade below z_0 due to inelastic losses increasing along with the neutral density.

4. Descending Artificial Ionized Layer (DAIL)

[18] A model of the development of newly ionized (artificial) plasma involves the spatial and temporal evolution of ionospheric electrons and four ion species, O^+, NO^+, O_2^+, and N_2^+. The main chemical processes included in the model are ionization of atomic and molecular oxygen and nitrogen by the accelerated electrons, production of molecular oxygen ions and nitrogen monoxide ions via charge exchange collisions, $O^+ + O_2 \rightarrow O_2^+ + O$ and $O^+ + N_2 \rightarrow NO^+ + N$, respectively, and recombination between electrons and molecular ions [e.g., *Schunk and Nagy*, 2000]. The resulting system of equations includes

$$\frac{\partial n}{\partial t} = k_{ion} N_n \frac{1}{n_e^0} - n\frac{n_{NO^+}}{\tau_{rec}^{NO^+}} - n\frac{n_{O_2^+}}{\tau_{rec}^{O_2^+}} - n\frac{n_{N_2^+}}{\tau_{rec}^{N_2^+}} - \frac{n}{\tau_d} \tag{10}$$

$$\frac{\partial n_{O^+}}{\partial t} = k_{ion}^O N_O \frac{1}{n_e^0} - \frac{n_{O^+}}{\tau_{exc}^{(1)}} - \frac{n_{O^+}}{\tau_{exc}^{(2)}} - \frac{n_{O^+}}{\tau_d} \tag{11}$$

$$\frac{\partial n_{NO^+}}{\partial t} = \frac{n_{O^+}}{\tau_{exc}^{(1)}} - n\frac{n_{NO^+}}{\tau_{rec}^{NO^+}} - \frac{n_{NO^+}}{\tau_d} \tag{12}$$

$$\frac{\partial n_{O_2^+}}{\partial t} = k_{ion}^{O_2} N_{O_2} \frac{1}{n_e^0} + \frac{n_{O^+}}{\tau_{exc}^{(2)}} - n\frac{n_{O_2^+}}{\tau_{rec}^{O_2^+}} - \frac{n_{O_2^+}}{\tau_d} \tag{13}$$

$$\frac{\partial n_{N_2^+}}{\partial t} = k_{ion}^{N_2} N_{N_2} \frac{1}{n_e^0} - n\frac{n_{N_2^+}}{\tau_{rec}^{N_2^+}} - \frac{n_{N_2^+}}{\tau_d} \tag{14}$$

Table 1. Fitted Power Law Coefficients a and b as Functions of E_0 and T_e

E_0 (V/m)	T_e (eV)	a	b
1.0	0.4	0.0172	2.53
1.0	0.6	0.0380	2.36
1.0	0.8	0.0576	2.24
1.5	0.4	0.0189	2.02
1.5	0.6	0.0291	1.90
1.5	0.8	0.0371	1.82
2.0	0.4	0.0137	1.54
2.0	0.6	0.0174	1.46
2.0	0.8	0.0197	1.40

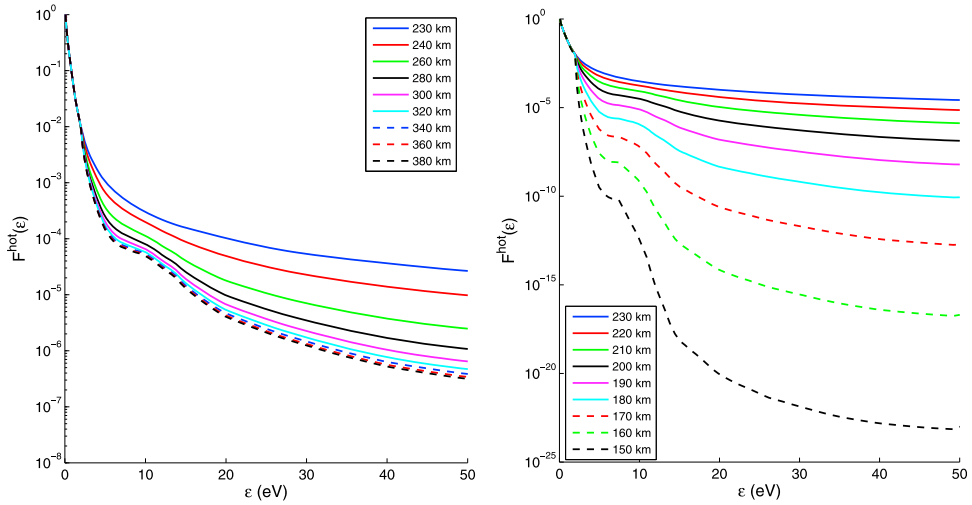

Figure 9. The electron energy distribution $F^{hot}(\varepsilon,z)$ at various altitudes (a) above and (b) below the acceleration region for $E_O = 1.5$ V/m and $T_{e0} = 0.6$ eV.

Here $n = n_e(z,t)/n_e^0$, $n_{O^+} = N_{O^+}(z,t)/n_e^0$, $n_{NO^+} = N_{NO^+}(z,t)/n_e^0$, $n_{O_2^+} = N_{O_2^+}(z,t)/n_e^0$, and $n_{O_2^+} = N_{O_2^+}(z,t)/n_e^0$ are the normalized densities,

$$k_{ion}^j(z) = n_c \int_{\varepsilon_{ion}^j}^{\infty} \sqrt{\frac{2\varepsilon}{m_e}} \sigma_{ion}^j(\varepsilon,z) F^{hot}(\varepsilon,z) d\varepsilon \qquad (15)$$

is the coefficient of ionization of species j, $\sigma_{ion}^j(\varepsilon,z)$ is the ionization cross-section, τ_{rec}^j and $\tau_{exc}^{(1,2)}$ are the time scales for recombination and exchange collisions, respectively. We use $\tau_{rec}^{(1)} = (\alpha_{NO^+} n_e^0)^{-1}$, $\tau_{rec}^{(2)} = (\alpha_{O_2^+} n_e^0)^{-1}$, $\tau_{rec}^{(3)} = (\alpha_{N_2^+} n_e^0)^{-1}$, $\tau_{exc}^{(1)} = 1/(\beta_1 N_{N_2})$, and $\tau_{exc}^{(2)} = 1/(\beta_2 N_{O_2})$, where $\alpha_{NO^+} = 3.5 \times 10^{-7} (T_0/T_e)^{0.69}$ cm^3/s, $\alpha_{O_2^+} = 1.95 \times 10^{-7} (T_0/T_e)^{0.7}$ cm^3/s, $\alpha_{N_2^+} = 2.2 \times 10^{-7} (T_0/T_e)^{0.39}$ cm^3/s, $\beta_1 = 1.2 \times 10^{-12}$ cm^3/s, and $\beta_2 = 2.1 \times 10^{-11}$ cm^3/s [*Schunk and Nagy*, 2000].

[19] Plasma decay due to ambipolar diffusion is accounted for by including the terms with the decay time $\tau_d = L_N^2/D_A$ in the right-hand side of the system (10)–(14). Here $D_A = (1 + T_e/T_i) k_B T_i / m_i \nu_{in}$ is the ambipolar diffusion coefficient, $\nu_{in} = C_{in} N_n$, $N_n = N_O + N_{O_2} + N_{N_2}$ is the total neutral density, and $L_N = 1/(d \ln N_n/dz)$ is the length-scale of the neutral gas. For simplicity, $C_{in} = 4 \times 10^{-10}$ cm^{-3}/s is taken for all ion species. The total ionization rate for electrons $k_{ion} N_n = k_{ion}^O N_O + k_{ion}^{O_2} N_{O_2} + k_{ion}^{N_2} N_{N_2}$ defines the ionization time scale $\tau_{ion} = n_e/(k_{ion} N_n)$.

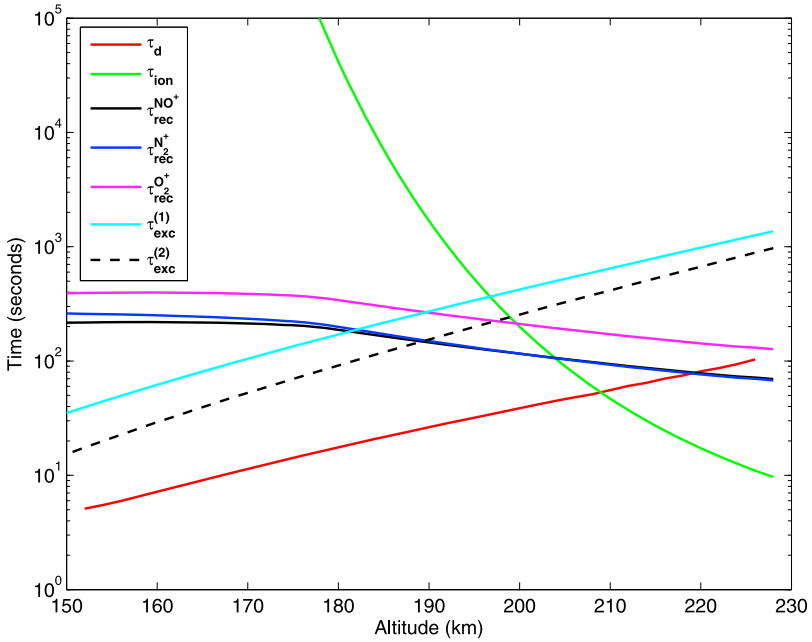

Figure 10. The diffusion, ionization, recombination, and charge exchange times vs. altitude for the acceleration region at $z_0 = 230$ km, $E_O = 1.5$ V/m, and $T_{e0} = 0.6$ eV.

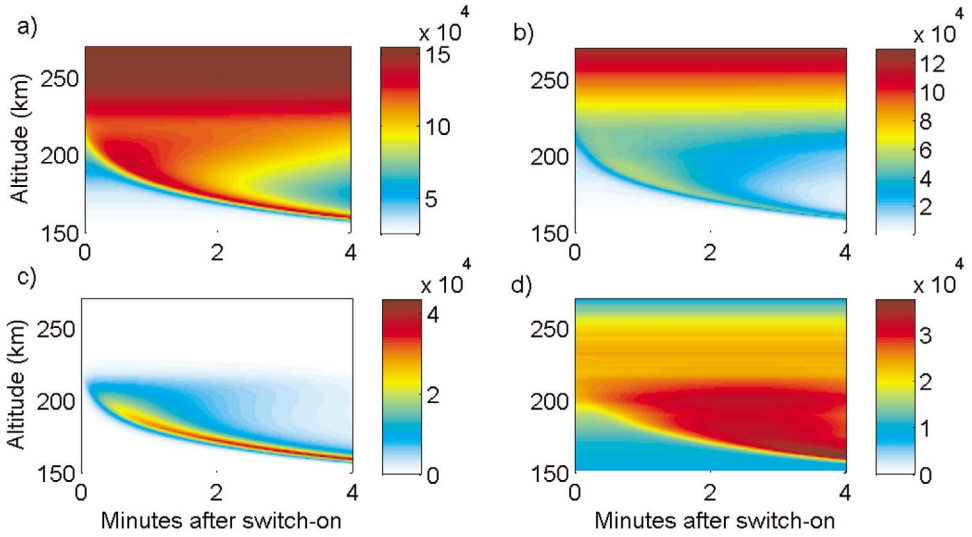

Figure 11. Time-vs-altitude plots of the densities in cm^{-3} of (a) electrons, (b) O^+ ions, (c) N_2^+ ions, and (d) O_2^+ ions, for $E_O = 1.5$ V/m, and $T_{e0} = 0.6$ eV.

The quasi-neutrality condition $n_e(z, t) = N_{O^+}(z, t) + N_{NO^+}(z, t) + N_{O_2^+}(z, t) + N_{N_2^+}(z, t)$ is assumed.

[20] Figure 10 shows the time scales for ionization, recombination, charge exchange collisions, and diffusion as functions of altitude calculated below the acceleration region near $z_0 = 230$ km using $F^{hot}(\varepsilon, z)$ from Figure 9b. The ionization rate $\sim 1/\tau_{ion}$ decreases dramatically at lower altitudes due to the rapid degradation of the fast electron population, as seen in Figure 9b. This limits the region of the newly produced (artificial) plasma by the average degradation length of the ionizing ($\varepsilon > \varepsilon_{ion}^j$) fast electrons.

[21] The solution of the system (10)–(15) is consistent with the *Mishin and Pedersen* [2011] ionizing wavefront scenario. The SLT acceleration region (layer) is located just below the turning point z_O of the pump wave defined by the matching of the pump frequency to the local plasma frequency or $n_e = n_c$. As the new plasma builds up, the matching condition is reached somewhere at $z = z_s < z_O$ defined by the matching condition $n_e(z_s) = n_c$. Then, SLT develops within the new layer, and the aforesaid acceleration/ionization process is repeated again and again, every time at lower altitudes adjacent to $z_s(t)$. In the simulation, a 4th-order Runge-Kutta scheme for the time stepping is

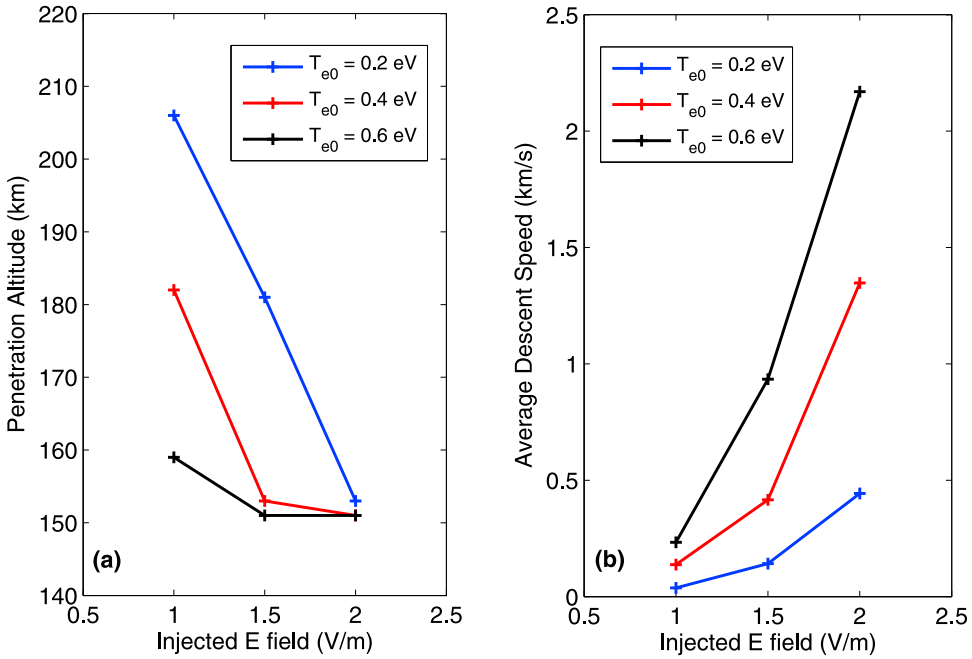

Figure 12. (a) Scaling of the final DAIL position and (b) average descent speed vs. injected wave amplitude for three different initial electron temperatures.

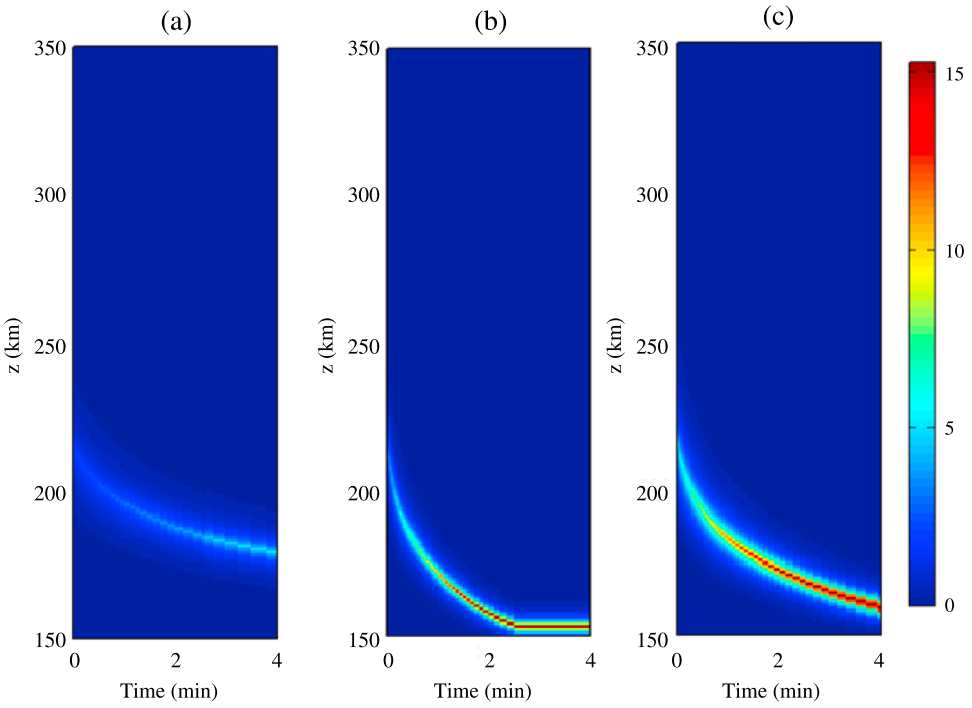

Figure 13. Green line emission as derived from simulation for different input wave amplitude and initial electron thermal energy: (a) E_0 = 1 V/m, T_e = 0.4 eV, (b) E_0 = 1.5 V/m, T_e = 0.4 eV, and (c) E_0 = 1 V/m, T_e = 0.6 eV.

applied with a 0.1 s time step and a spatial grid of 0.5 km. The location of the accelerating layer, initially at 230 km, is dynamically updated at each time step. We assume that SLT produces the same power-law distribution at each step.

[22] Figure 11 shows the temporal and spatial development of the densities of electrons, O^+ and molecular ions. It is seen that in 4 minutes the artificial plasma descends from 230 to ≈160 km with the mean speed ≈300 m/s. Initially, the electron and O^+ densities increase in step due to ionization of mainly atomic oxygen, which is the dominant component at $z > 180$ km. At lower altitudes, the formation of the artificial plasma is dominated by ionization of nitrogen. The ionospheric length scale L_n at the critical layer typically decreases from about 40 km in the original ionosphere, to about 10 km at lower altitudes. Near the terminal altitude of 150 km, the ionization production (cf. Figure 10) and speed of descent slow down. At the terminus, the ionization production is balanced mainly by recombination of molecular ions, and the descent stops.

[23] Figure 12 shows the DAIL terminal altitude (Figure 12a) and the average descent speed (Figure 12b) computed for different values of E_O and T_{e0}. The average speed is simply the distance from the initial altitude to the terminus divided by the propagation time. At relatively low E_O = 1 V/m and T_{e0} = 0.2 eV, the DAIL descends by less than 10 km. For lower pump electric fields and electron temperatures, DAILs do not develop. As anticipated from the dependence of the ionization rate, the average speed increases with E_O and T_{e0}.

[24] To compare directly with the DAIL optical signatures [*Pedersen et al.*, 2010], the green-line emissions have been calculated from the simulation data. As in the experiment, the green-line emission serves as diagnostics of the related DAIL. Figure 13 shows the results of modeling of the relative intensity of the oxygen emission at 557.7 nm (the green line) excited by the accelerated electrons. The emission intensity I is proportional to the excitation rate of atomic oxygen by the electron impact $I \propto N_O \int_{4.2\text{ eV}}^{\infty} F^{hot}(\varepsilon,z)\sigma_{1S}(\varepsilon,z)\nu(\varepsilon)d\varepsilon$. Here σ_s is the excitation cross section of the $O(1S)$ state. As with the descent speed, the intensity increases with the pump electric field and the temperature of the bulk of electrons.

5. Discussion

[25] In this section, we compare the simulation results with the observed features of HF-induced plasma layers. The simulations produce an artificial ionospheric layer, descending from ≈230 km on average at ≈300 m/s, until ionization is balanced by recombination and ambipolar diffusion near 150 km. As it follows from Figure 11a, during the first 2 min in the heating, the O^+-dominated newly born plasma at $h \geq 180$ km is confined to the bottomside of the original F_2 layer. At lower altitudes, the artificial plasma above the descending acceleration-ionization source is rapidly depleted due to recombination of molecular ions, thereby separating the ionization front from the original F_2 peak. These features agree well with the *Pedersen et al.* [2010] ionosonde and optical observations. The corresponding descent of the SLT generation region is also observed by the MUIR radar ion-line observations [*Mishin and Pedersen*, 2011, Figure 1].

[26] The low-amplitude threshold of E_O for the formation of DAILs seen in Figure 12a is in line with the recent observations at HAARP [*Pedersen*, 2012] which show that

DAILs have a threshold that appears to be somewhere between 1/3 and 1/2 HAARP full power, and under relatively low-amplitude electric fields, weak DAILs are formed slightly below the heating wave reflection point.

[27] On the other hand, Figure 12b revealed that the average descent speed of the DAIL increases with the injected electric field and the temperature of the bulk of electrons. *Mishin and Pedersen* [2011] showed that in their experiments the average descent speed was about 0.3 km/s. In our model this value corresponds to the field range between 1.1–1.4 V/m while the electron temperature ranges between 0.6–0.4 eV. A descent speed of 0.3 km/s also occurs at electron temperatures as low as 0.2 eV when the electric field is about 1.8 V/m. This provides an estimate for the range of parameters required to form DAILs such as observed at HAARP.

[28] We conclude that the salient observational features of the artificial plasma layers are well reproduced by the simulated ionization front created by the SLT-accelerated electron population. However, the observed and modeled ionospheric length scales L_n differ significantly at $h < 180$ km. The cause of that is the assumption that at each step the same distribution is produced. At low altitudes, as noted by *Mishin and Pedersen* [2011], the maximum energy of the accelerated electrons can be limited by inelastic losses that peak at $\varepsilon = \varepsilon_{\max} < 100$ eV. For the ionization layer to stop descending, the total rate of inelastic collisions $\nu_{il}(\varepsilon_{\max}) \cong 3 \times 10^{-7} N_n \sqrt{\beta}/(\beta+8)$ $(\beta = \varepsilon/\varepsilon_{ion})$ should exceed the acceleration rate of fast electrons $\gamma_a \sim D(v_{\max})/v_{\max}^2$ [*Volokitin and Mishin*, 1979]. Indeed, with $D(v)$ from Figure 5 for $E_O = 1\mathrm{V/m}$ we obtain that $\nu_{il} > \gamma_a$ at $N_n > 3 \times 10^{10}$ cm^{-3}, i.e. below about 160 km. Further, the pump amplitudes $E_O \geq 1$ V/m and electron temperatures $T_e \geq 0.4$ eV have been used to obtain the accelerated electron population. The enhanced T_e near the turning point z_O can be produced jointly by heating of ionospheric electrons directly by SLT and via fast electron thermal conduction from the upper hybrid layer [cf. *Pedersen et al.*, 2010]. However, the electron temperature is probably still too low for direct ionization due to bulk heating. Only electrons above a critical energy of about $\varepsilon_c = 12$ eV will contribute to the ionization. Integrating the Maxwellian electron distribution function for energies above this value, we obtain the fraction of the electron population above the critical energy as $\delta n_e(\varepsilon_c) \approx \sqrt{2\varepsilon_c/(\pi T_e)}$ $\exp[-\varepsilon_c/(2T_e)]$. To obtain $\delta n_e(\varepsilon_c) > 10^{-3}$ (a typical fraction produced by SLT), we need an electron temperature T_e above 1.5 eV, which is a few times higher than the values observed in the experiments. The remaining question is the value of E_O. The free-space electric field of the injected pump wave is $E_O \approx 5.5\sqrt{P_0}/R$ V/m at the effective radiative power P_0 (in MW) and distance R (in km). For $R = 200$ km, E_O reaches $\approx$1 V/m at $P_0 \approx 2.3$ GW, which is near the maximum for the upgraded HAARP transmitter at $f_0 \approx 7$ MHz. However, artificial layers [*Pedersen et al.*, 2010] have been observed at $f_0 = 2.85$ MHz and $P_0 \approx 440$ MW. A simple resolution to this quandary is accounting for background ("seed") suprathermal electrons, e.g., photoelectrons that can be accelerated much more efficiently than thermal electrons [e.g., *Mishin et al.*, 2004]. As soon as the ionizing front is established, the seed electron population near z_s will be maintained via degradation of the earlier-accelerated electrons streaming downward from z_s. We are currently expanding the code in order to include background suprathermal electrons into SLT acceleration and the pump fields increasing at lower altitudes with $1/R$.

[29] In summary, we have presented a multi-scale model for the generation and descent of artificial layers by high-power HF radio waves recently observed at HAARP. The model includes a complete wave model of the ionospheric turbulence, from which an effective diffusion coefficient is derived and used in a Fokker-Planck model for electron acceleration due to resonant wave-particle interactions. The transport of the hot electrons is modeled with a kinetic model, and a dynamic model is developed to describe the creation and descent of the artificial ionospheric layers.

[30] **Acknowledgments.** The work at UMD was supported by DARPA via a subcontract N684228 with BAE Systems and also by MURI N000140710789. E.V.M. was supported by the Air Force Office of Scientific Research. B.E. acknowledges partial support by the DFG FOR1048 (Bonn, Germany).

[31] Robert Lysak thanks the reviewers for their assistance in evaluating this paper.

References

Carlson, H. C., Jr. (1993), High-power HF modification: Geophysics, span of EM effects, and energy budget, *Adv. Space Res.*, *13*(10), 15–24, doi:10.1016/0273-1177(93)90046-E.

DuBois, D. F., H. A. Rose, and D. Russell (1990), Excitation of strong Langmuir turbulence in plasmas near critical density: Application to HF heating of the ionosphere, *J. Geophys. Res.*, *95*, 21,221–21,272, doi:10.1029/JA095iA12p21221.

Eliasson, B. (2008a), A nonuniform nested grid method for simulations of RF induced ionospheric turbulence, *Comput. Phys. Commun.*, *178*, 8–14, doi:10.1016/j.cpc.2007.07.008.

Eliasson, B. (2008b), Full-scale simulation study of the generation of topside ionospheric turbulence using a generalized Zakharov model, *Geophys. Res. Lett.*, *35*, L11104, doi:10.1029/2008GL033866.

Eliasson, B., and L. Stenflo (2008), Full-scale simulation study of the initial stage of ionospheric turbulence, *J. Geophys. Res.*, *113*, A02305, doi:10.1029/2007JA012837.

Eliasson, B., and L. Stenflo (2010), Full-scale simulation study of electromagnetic emissions: The first ten milliseconds, *J. Plasma Phys.*, *76*, 369–375, doi:10.1017/S0022377809990559.

Galeev, A. A., R. Z. Sagdeev, V. D. Shapiro, and V. I. Shevchenko (1977), Langmuir turbulence and dissipation of high-frequency energy, *Sov. Phys. JETP, Engl. Transl.*, *46*, 711–728.

Galeev, A., R. Sagdeev, V. Shapiro, and V. Shevehenko (1983), Beam plasma discharge and suprathermal electron tails, in *Active Experiments in Space (Alpbach, Austria)*, *Eur. Space Agency Spec. Publ.*, *ESA SP-195*, 151–155.

Gurevich, A. (1978), *Nonlinear Phenomena in the Ionosphere*, Springer, New York, doi:10.1007/978-3-642-87649-3.

Gurevich, A. V., Y. S. Dimant, G. M. Milikh, and V. V. Vas'kov (1985), Multiple acceleration of electrons in the regions of high-power radio-wave reflection in the ionosphere, *J. Atmos. Terr. Phys.*, *47*, 1057–1070, doi:10.1016/0021-9169(85)90023-6.

Gurevich, A. V., H. C. Carlson, Y. V. Medvedev, and K. P. Zybin (2004), Langmuir turbulence in ionospheric plasma, *Plasma Phys. Rep.*, *30*, 995–1005, doi:10.1134/1.1839953.

Hansen, J. D., G. J. Morales, L. M. Duncan, J. E. Maggs, and G. Dimonte (1990), Large-scale ionospheric modifications produced by nonlinear refraction of an hf wave, *Phys. Rev. Lett.*, *65*, 3285–3288, doi:10.1103/PhysRevLett.65.3285.

Koert, P. (1991), Artificial ionospheric mirror composed of a plasma layer which can be tilted, Patent 5,041,834, U.S. Patent and Trademark Off., Washington, D. C.

Kosch, M. J., M. T. Rietveld, A. Senior, I. W. McCrea, A. J. Kavanagh, B. Isham, and F. Honary (2004), Novel artificial optical annular structures in the high latitude ionosphere over EISCAT, *Geophys. Res. Lett.*, *31*, L12805, doi:10.1029/2004GL019713.

Manheimer, W. M., and K. Papadopoulos (1975), Interpretation of soliton formation and parametric instabilities, *Phys. Fluids*, *18*, 1397–1398, doi:10.1063/1.861003.

Mjølhus, E. (1990), On linear conversion in a magnetized plasma, *Radio Sci.*, *25*, 1321–1339, doi:10.1029/RS025i006p01321.

Mjølhus, E., E. Helmersen, and D. DuBois (2003), Geometric aspects of HF driven Langmuir turbulence in the ionosphere, *Nonlinear Processes Geophys.*, *10*, 151–177, doi:10.5194/npg-10-151-2003.

Mishin, E., and T. Pedersen (2011), Ionizing wave via high-power HF acceleration, *Geophys. Res. Lett.*, *38*, L01105, doi:10.1029/2010GL046045.

Mishin, E. V., W. J. Burke, and T. Pedersen (2004), On the onset of HF-induced airglow at HAARP, *J. Geophys. Res.*, *109*, A02305, doi:10.1029/2003JA010205.

Morales, G. J., and Y. C. Lee (1974), Effect of localized electric fields on the evolution of the velocity distribution function, *Phys. Rev. Lett.*, *33*, 1534–1537, doi:10.1103/PhysRevLett.33.1534.

Papadopoulos, K., and T. Coffey (1974), Nonthermal features of the auroral plasma due to precipitating electrons, *J. Geophys. Res.*, *79*, 674–677, doi:10.1029/JA079i004p00674.

Pedersen, T. (2012), Artificial ionospheric layers: Recent progress and propagation effects, paper presented at RF Ionospheric Interactions Workshop, Natl. Sci. Found., Santa Fe, N. M., April.

Pedersen, T., B. Gustavsson, E. Mishin, E. MacKenzie, H. C. Carlson, M. Starks, and T. Mills (2009), Optical ring formation and ionization production in high-power HF heating experiments at HAARP, *Geophys. Res. Lett.*, *36*, L18107, doi:10.1029/2009GL040047.

Pedersen, T., B. Gustavsson, E. Mishin, E. Kendall, T. Mills, H. C. Carlson, and A. L. Snyder (2010), Creation of artificial ionospheric layers using high-power HF waves, *Geophys. Res. Lett.*, *37*, L02106, doi:10.1029/2009GL041895.

Pelletier, G. (1982), Generation of a high-energy electron tail by strong Langmuir turbulence in plasma, *Phys. Rev. Lett.*, *49*, 782–785, doi:10.1103/PhysRevLett.49.782.

Sagdeev, R., and A. Galeev (1969), *Nonlinear Plasma Theory*, Benjamin, New York.

Schunk, R. W., and A. N. Nagy (2000), *Ionospheres - Physics, Plasma Physics and Chemistry*, Cambridge Univ. Press, New York, doi:10.1017/CBO9780511551772.

Volokitin, A., and E. Mishin (1979), Relaxation of an electron beam in a plasma with infrequent collisions, *Sov. J. Plasma Phys.*, *5*, 654–656.

Wang, J., D. Newman, and M. Goldman (1997), Vlasov simulations of electron heating by Langmuir turbulence near the critical altitude in the radiation-modified ionosphere, *J. Atmos. Sol. Terr. Phys.*, *59*, 2461–2474, doi:10.1016/S1364-6826(96)00140-X.

Zakharov, V. (1984), Collapse and self-focusing of Langmuir waves, in *Basic Plasma Physics*, vol. 2, edited by A. Galeev and R. Sudan, pp. 81–121, North-Holland, New York.